

PdFe Alloy- Fe_5C_2 interfaces for efficient CO_2 hydrogenation to higher alcohols

Yanqiu Wang^{a,1}, Ying Zhou^{a,1}, Xinxin Zhang^a, Mingrui Wang^b, Tangkang Liu^a, Jinxing Wei^a, Guanghui Zhang^{b,*}, Xinlin Hong^{a,*}, Guoliang Liu^{c,a,**}

^a College of Chemistry and Molecular Sciences, Wuhan University, Wuhan 430072, PR China

^b State Key Laboratory of Fine Chemicals, PSU-DUT Joint Center for Energy Research, School of Chemical Engineering, Dalian University of Technology, Dalian 116024, PR China

^c Interdisciplinary Institute of NMR and Molecular Sciences, School of Chemistry and Chemical Engineering, Wuhan University of Science and Technology, Wuhan 430081, PR China



ARTICLE INFO

Keywords:

Heterogeneous catalysis
Carbon dioxide hydrogenation
PdFe alloy
Higher alcohols
Synergetic mechanism

ABSTRACT

Direct CO_2 hydrogenation to higher alcohols (HA) is a promising route for high-value utilization of waste CO_2 , but developing active and stable catalysts remains a grand challenge. For this reaction, constructing multi-functional interfaces as active sites is required to fulfill controllable C-C coupling of alkyl and $\text{CO}^*/\text{CH}_x\text{O}^*$ species. Herein, we report a PdFe catalyst with abundant PdFe alloy- Fe_5C_2 interfaces via a PdFe alloy induced FeO_x carbidization process, which can achieve HA yield of $86.5 \text{ mg g}_{\text{cat}}^{-1} \text{ h}^{-1}$ with 26.5% selectivity at 300°C , 5 MPa, and $6000 \text{ mL g}_{\text{cat}}^{-1} \text{ h}^{-1}$. The accelerated deactivation test unveils the PdFe catalyst exhibits better durability than the widely studied CuFe based catalysts against harsh conditions. Multiple in-situ characterization results unveil a synergetic mechanism for HA synthesis at the PdFe alloy- Fe_5C_2 interfaces, where PdFe alloy is responsible for CO formation and non-dissociative activation, while Fe_5C_2 phase promotes CO dissociation and chain propagation.

1. Introduction

Converting carbon dioxide (CO_2) into chemicals and energy feedstocks is a promising approach to recycling the massive CO_2 released during industrial processes. The hydrogenation of CO_2 by “green” hydrogen (H_2 , produced by renewable energy such as solar energy, wind power, and biomass) is of great significance to alleviate the demand for clean fuels [1]. Higher alcohols (HA), containing two or more carbon atoms, are suitable to be applied either as fuel additives for octane enhancement or as pure fuels in existing internal combustion engines, which has attracted considerable attention [2,3]. Over the past few decades, there has been intensive research focusing on shifting the synthesis from hydrocarbons and methanol towards C_{2+} oxygenates in consideration of high atom economy and improved product value [4]. However, the chemical inertness of the CO_2 molecule and the difficulty in C-C coupling reaction make controllable higher alcohol synthesis

(HAS) a grand challenge [5,6]. Thus far, the state-of-the-art HA productivity for gas-phase CO_2 hydrogenation is still far from satisfactory. Accordingly, substantial catalytic advances are urgently required for the efficient hydrogenation of CO_2 to HA.

The production rate of HA is determined by the key step of C-C coupling of alkyl species and CO^* (so-called CO insertion) [7–9], which requires the multifunctional interfaces with both dissociative and non-dissociative C-O bond activations [10–13]. In contrast to syngas conversion, the reaction atmosphere of CO_2 hydrogenation has an extremely low CO/H_2 ratio and high partial pressure of water vapor, bringing huge challenges for constructing and stabilizing the active interfaces under working conditions [14–16]. The catalysts for HAS from CO_2 hydrogenation mainly include Rh, Co, Fe-based catalysts, etc. Among them, Fe-based catalysts are found to be practically promising, because of high CO_2 conversion and high HA production rate [17–19]. Numerous studies have demonstrated that iron carbide (FeC_x) phase is

* Corresponding authors.

** Corresponding author at: Interdisciplinary Institute of NMR and Molecular Sciences, School of Chemistry and Chemical Engineering, Wuhan University of Science and Technology, Wuhan 430081, PR China.

E-mail addresses: gzhang@dlut.edu.cn (G. Zhang), hongxl@whu.edu.cn (X. Hong), liugl@whu.edu.cn (G. Liu).

¹ These authors have contributed equally to this work.

very active for C–O bond dissociation and its chain-propagation probability is not that much sensitive to low CO partial pressure [20]. This renders FeC_x-based catalysts as the most appealing option for the synthesis of C₂₊ alcohols from CO₂/H₂. When FeC_x is modified with M sites (for example, Cu, in charge of non-dissociative CO activation) to form M–FeC_x interfaces, the HAS activity would be facilitated. We previously demonstrated that the HAS activity at the M–FeC_x interfaces relies on the balance of dissociative and nondissociative C–O bond activation in synergy [21,22]. However, the rapid deactivation caused by the sintering of M (e.g., Cu) under harsh reaction conditions impedes the practical use. Thus, it is urgent to develop stable FeC_x-containing active interfaces to realize the efficient HAS.

Pd-based catalysts hold great potential for alcohol synthesis because of the good activity of non-dissociative C–O bond activation [23]. Monoatomic Pd/Fe₃O₄ and Pd dimer/CeO₂ were recently reported for ethanol production, but the sintering of single/dimer Pd atoms leads to severe catalyst deactivation under harsh conditions (i.e., reductive H₂-rich atmosphere) [24,25]. Recently, a water-enriched environment was employed to stabilize Pd dimer by increasing the energy barrier of Pd atoms' migration [26]. However, the suppression of atom aggregation under a H₂-rich environment is still an important problem faced by single atom catalysts. Nano-particulate Pd is more robust but easily poisoned by CO due to its strong affinity to CO binding [27]. Alloying Pd with other metals (e.g., Fe, Co, Zn, Ga) can lower the energy level of filled Pd 4d valance band states, thus resulting in the weakening of CO adsorption and poisoning. It is also reported that the valence electronic densities of states of some Pd alloys (e.g., PdZn) fulfill the necessary functionality in non-dissociative C–O bond activation for C₂₊ alcohol synthesis [28,29]. It is reasonable to speculate that the production of HA with improved activity and stability could be achieved at the Pd alloy–iron carbide interfaces. Herein, we report the fabrication of well-defined PdFe alloy–Fe₅C₂ interfaces through in-situ evolution of Fe₂O₃ supported Pd catalysts for efficient and stable CO₂ hydrogenation to HA. We demonstrate that the formed PdFe alloy upon H₂ reduction can further promote the complete carbidization of Fe species to active Fe₅C₂ phase, thus forming abundant PdFe alloy–Fe₅C₂ interfaces. The synergy between PdFe alloy and Fe₅C₂ enables efficient CO₂ conversion to HA, with selectivity of 26.5% and STY of 86.5 mg g_{cat}⁻¹ h⁻¹ under reaction conditions of 300 °C, 5 MPa, and 6 L g⁻¹ h⁻¹. This performance has ranked the top among the Pd/Fe-based catalysts in the literature.

2. Experimental procedures

2.1. Catalyst synthesis

The Fe₂O₃ support was prepared by using a propylene oxide assisted hydrothermal method. Briefly, 5.656 g of Fe(NO₃)₃·9 H₂O (AR, Aladdin) was dissolved into 50 mL of ethanol (AR) by ultrasound. Then 2 mL of 1, 2-propylene oxide (AR, Sinopharm Chemical Reagent) was added into the Fe³⁺ solution with magnetic stirring rapidly for 10 min. The mixture was heated at 150 °C in an oven for 20 h followed by dried at 60 °C for 24 h and 200 °C for 3 h. The final solid powder was calcined in a muffle furnace for 4 h at 600 °C (5 °C min⁻¹) getting Fe₂O₃ material. The other Fe₂O₃ supports with different particle sizes was prepared by a modified PVP sol-gel method. Typically, 3.03 g of Fe(NO₃)₃·9 H₂O (AR, Aladdin) was dissolved in 2.5 mL of deionized water. The ionic solution was dropped into a 10 wt% PVP aqueous solution. The mixture was stirred at room temperature for 2 h. The water is then dried completely in a 100 °C oven. After drying and cooling to room temperature, the collected products were ground in a mortar to powder. It was then heated to 150 °C at a rate of 2 °C min⁻¹ for 2 h and then heated to 350 °C at a rate of 2 °C min⁻¹ for 4 h in a muffle furnace. The final solid powder was named Fe₂O₃(x nm) according to the size of the Fe₂O₃ particle.

Different metal catalysts (M=Pd, Pt, Ag, and Ru) supported on Fe₂O₃ were prepared by an incipient wetness impregnation method. The catalysts are denoted as MFe-x, where x% stands for the loading of M in

mass fraction. For the typical synthesis of PdFe-x catalysts, a certain volume of Pd(NO₃)₂·2 H₂O (AR, Sinopharm Chemical Reagent) solution determined by Pd load was added dropwise to 0.3 g of Fe₂O₃ support with constant stirring. The impregnation lasted for 5 h under ambient temperature followed by evaporation at 120 °C. After dried at 80 °C, the powder was calcined at 300 °C for 2 h at a ramp rate of 1 °C min⁻¹ getting PdFe-x. For the reference 6.9 Pd/Al₂O₃ catalyst, commercial γ-Al₂O₃ was used to replace the Fe₂O₃ supports.

PdFe alloy supported on SBA-15 was prepared according to the literature [30]. The selected carrier was SBA-15 and the decomposition temperature was 300 °C. The obtained catalyst is denoted as PdFe/SBA-15 where the mass fraction of PdFe alloy is 20%, and the atomic ratio of Pd to Fe is controlled at 1:1. Pd₁Fe₂₀/SBA-15 was obtained by changing the atomic ratio of Pd to Fe to 1:20, where the mass fraction of Pd and Fe₃O₄ is 30%.

2.2. Catalyst characterization

X-ray powder diffraction (XRD) patterns were obtained by Bruker D8 Advance X-ray powder diffractometer. The electronic state of elements in catalysts was analyzed by X-ray photoelectron spectroscopy (XPS) on a Thermo ESCALAB 250Xi spectrometer. High-resolution transmission electron microscopy (HRTEM) images were obtained by a Tecnai G2 F30 S-TWIN electron microscope. HAADF-STEM images were obtained on a JEM ARM 200 F electron microscope.

H₂ temperature-programmed reduction (H₂-TPR), CO temperature-programmed surface reaction (CO-TPSR), H₂ and CO₂ temperature-programmed desorption (H₂/CO₂-TPD), CO pulse transient hydrogenation experiments were carried out on a Micromeritics Autochem ASSP-2920 chemisorption analyzer equipped with a thermal conductivity detector (TCD) and a quadrupole mass spectrometer (MS) detector (Hidden, QIC-20). For H₂-TPR, 30 mg of sample was treated at 150 °C under Ar (30 mL min⁻¹) for 1 h. After cooling down to 50 °C, the gas was switched to 5 vol% H₂/Ar and the sample was heated to 800 °C with a heating rate of 10 °C min⁻¹. The signal was recorded by TCD simultaneously. For H₂-TPD, 30 mg of samples were reduced at 350 °C for 1 h under 5% vol H₂/Ar stream (30 mL min⁻¹) followed by cooled down to 50 °C. Then Ar was used to purge the residual H₂ for 30 min under a flow of 50 mL min⁻¹. After that, TPD measurements were conducted from 50 to 800 °C with a heating rate of 10 °C min⁻¹ in Ar stream, and the signal of *m/z* = 2 (H₂) was recorded by MS simultaneously. For CO₂-TPD, 30 mg of samples were reduced at 350 °C for 1 h in 5% vol H₂/Ar stream (30 mL min⁻¹) and flushed by Ar stream (50 mL min⁻¹) for 30 min. When the sample was cooled to 50 °C, the gas was switched to CO₂ for pre-adsorption lasting for 30 min. Ar was then used to purge the residual CO₂ under a flow of 50 mL min⁻¹ for 30 min. TPD measurements were then conducted from 50 to 800 °C with a heating rate of 10 °C min⁻¹ in Ar stream, and the signal of *m/z* = 44 (CO₂) was recorded by MS simultaneously. For CO-TPSR, the sample was reduced at 350 °C for 1 h under 5% vol H₂/Ar flow. After cooling down to ambient temperature, the sample was exposed to CO for pre-adsorption lasting for 30 min, and flushed with Ar for 30 min. Finally, the gas was switched to 5% vol H₂/Ar and the sample was heated to 800 °C with a ramp rate of 10 °C min⁻¹. TCD detector and MS detector were used to detect the signals simultaneously. For CO pulse transient hydrogenation experiment, the spent catalyst was reduced at 350 °C for 1 h under 5% vol H₂/Ar flow, and then switched to Ar for 1 h. After cooling down to 320 °C, CO pulse was imported into the reactor for serval cycles with an interval time of 15 min under 5 vol% H₂/Ar stream (30 mL min⁻¹). The MS signals of CO, CH₄, CH₃CHO, and CH₃CH₂OH were collected.

In situ diffuse reflectance infrared Fourier transform spectroscopy (DRIFTS) measurements were conducted on a Bruker VERTEX 70 spectrometer equipped with an MCT detector. For in situ DRIFTS of CO adsorption, the sample was firstly reduced at 120 °C or 350 °C under 10% H₂/Ar stream (30 mL min⁻¹) and then purged with Ar for 1 h. When the system was cooled to 35 °C the background spectrum was collected.

The gas was then switched to 5% CO/Ar lasting for 30 min. After that Ar stream with a flow of 30 mL min⁻¹ was used to sweep the adsorbed sample for 30 min. At last, the infrared spectrum of the sample with CO stably absorbed was collected. For in situ DRIFTS of CO₂ hydrogenation, the sample was reduced at 350 °C in 10% H₂/Ar flow for 1 h, and then purged with Ar for 1 h. When the system was cooled to 300 °C, the background spectrum was collected. The gas was then switched to CO₂/H₂ (1/3) mixture with a flow of 30 mL min⁻¹ at 0.3 MPa and the time-resolved DRIFTS spectra were collected synchronously. For in situ DRIFTS of hydroformylation reaction, the sample was reduced at 350 °C in 10% vol H₂/Ar flow for 1 h, and then purged with Ar for 1 h. When the system was cooled to 280 °C, the background spectrum was collected. The gas was then switched to ethylene with a flow of 30 mL min⁻¹ at 0.4 MPa for 30 min. When the spectrum remained stable, the gas was switched to syngas with a flow of 30 mL min⁻¹ at 0.4 MPa and the time-resolved DRIFTS spectra were collected synchronously.

In situ XRD experiments were carried out in an XRK900 reactor chamber (Anton-Paar Corporation) equipped in a diffractometer. The solid powder was pressed into a pellet and then packed into a ceramic sample stage. Typically, 10% H₂/N₂ flow was fed at a flow rate of 30 mL min⁻¹ at 350 °C for the reduction process. Then, the feed gas was switched to the reactant gas (CO₂/H₂ = 1/3) at a flow rate of 20 mL min⁻¹. The XRD sample chamber was pressurized to 0.8 MPa and the reaction temperature was controlled at 320 °C. The patterns were collected simultaneously.

H₂-D₂ exchange experiments were carried out on a Micromeritics Autochem ASSP-2920 chemisorption analyzer. Typically, 15 mg of catalyst was placed into a U-shaped quartz tube and reduced at 350 °C for 1 h in a 10% H₂/Ar flow (30 mL min⁻¹) with a heating rate of 5 °C min⁻¹, followed by cooling down to 150 °C. Then D₂ (30 mL min⁻¹) mixed with H₂ (30 mL min⁻¹) was introduced into the reactor, and the signals were recorded by a mass spectrometer detector (MS, Hidden, QIC-20), with the *m/z* signals of 2 (H₂), 4 (D₂) and 3 (HD).

2.3. Catalytic testing

The catalytic performances of CO₂ hydrogenation were evaluated on a tubular fixed-bed continuous-flow microreactor. Before the test, 0.2 g of catalyst was evenly distributed over the quartz cotton in the reaction tube at an appropriate height. The catalyst was pre-reduced under 10% vol H₂/Ar stream with a flow rate of 30 mL min⁻¹ at 350 °C for 1 h under atmospheric pressure. When the reactor was cooled down to about 320 °C, a CO₂/H₂/N₂ (24/72/4) mixture was fed into the reactor and the pressure was controlled at 5 MPa. The gas hourly space velocity (GHSV) was set at 6 L·g⁻¹·h⁻¹ and different reaction temperature (320 and 300 °C) was investigated. All data were obtained after the reaction lasts for 3 h at each temperature for the equilibrium of effluent product compositions. The effluent products were monitored online with a gas chromatography equipped with a thermal conductivity detector (TCD) and flame ionization detector (FID) simultaneously.

The CO₂ conversion, CO selectivity, CO-free products selectivity, and higher alcohols fraction (C₂₊OH/ROH) were calculated according to the following equations:

$$\text{CO}_2 \text{ Conversion} = \frac{A_{\text{CO}_2,\text{in}} - A_{\text{CO}_2,\text{out}}}{A_{\text{CO}_2,\text{in}}} \times 100\%$$

where A_{CO_{2,in}} and A_{CO_{2,out}} stand for CO₂ peak areas in chromatogram at the inlet and outlet, respectively.

$$\text{CO Selectivity} = \frac{A_{\text{CO},\text{out}}}{A_{\text{CO}_2,\text{in}} - A_{\text{CO}_2,\text{out}}} \times 100\%$$

A_{CO,out} represents CO peak areas in chromatogram at the outlet.

$$\text{CO-free C}_i \text{ Selectivity} = \frac{C_{i,\text{out}} \times i}{\sum_{i=1}^n C_{i,\text{out}} \times i} \times 100\%$$

C_{i,out} stands for the mole of C_i at the outlet and i is the carbon

number of product C_i.

$$\text{C}_2+\text{OH / ROH Fraction} = \frac{\sum_{i=2}^n C_{i,\text{OH out}} \times M_i}{\sum_{i=1}^n C_{i,\text{OH out}} \times M_i} \times 100\%$$

C_i OH_{out} and M_i stand for the mole of C_i OH at the outlet and the molar mass of C_i OH, respectively.

3. Results and discussion

3.1. Catalytic performance of PdFe catalysts

A series of Fe₂O₃ supported Pd catalysts with different loading were prepared by an incipient wetness impregnation method. The final catalysts are encoded as PdFe-x (x = 0, 0.1, 0.9, 4.3, 6.9 and 10.4), where x % represents the loading of Pd in mass fraction. The catalysts were pre-reduced by H₂ at 350 °C and then tested under catalytic conditions of 300–320 °C, 5 MPa, H₂/CO₂/N₂ = 72/24/4, and 6 L g_{cat}⁻¹ h⁻¹. As seen from Fig. 1A, the pure Fe₂O₃ catalyst gives almost alkane selectivity (>94%), of which more than 60% is CH₄. When a small amount of Pd (<1 wt%) is loaded, the CH₄ selectivity drops, along with improved carbon chain growth ability (Fig. S1). The HAS activity still keeps at a very low level (Fig. 1B). When the Pd loading is higher than 4.3%, the selectivity of alkanes, especially CH₄, decreases while that of olefins increases significantly. Meanwhile, the selectivity and space-time yield (STY) of HA are improved remarkably. Notably, the PdFe-6.9 catalyst exhibits the best activity, with HA selectivity of 19.3% and STY of 61.5 mg g_{cat}⁻¹ h⁻¹ at 300 °C. Increasing reaction temperature to 320 °C, the HA STY can be further increased to 68.1 mg g_{cat}⁻¹ h⁻¹ but compromised by a reduction in the HA selectivity. The mass fraction of C₂₊ alcohols in the total alcohols is above 94%, which helps reduce separation cost. We can conclude that a proper amount of Pd (i.e., 6.9%) is decisive to the HAS activity. The activity of the Pd catalyst was then compared with other noble metal catalysts such as Pt, Ru, and Ag, and the catalytic results proved that the PdFe-6.9 catalyst presents special superiority in catalyzing CO₂ hydrogenation to HA (Fig. S2 and S3).

Over the PdFe-6.9 catalyst, further raising the gas hourly space velocity (GHSV), the HA STY goes up, reaching up to 105.1 mg g_{cat}⁻¹ h⁻¹ at 12 L g_{cat}⁻¹ h⁻¹ (Fig. S4). Meanwhile, the CO₂ conversion decreases while the CO selectivity increases, which suggests CO may act as the key intermediate in CO₂ hydrogenation reaction. The reaction pressure also influences the HAS activity kinetically. High pressure (5 MPa) is beneficial to the CO₂ conversion and HAS activity (Fig. S5). Besides, the accelerated deactivation test unveils that the PdFe-6.9 catalyst exhibits better durability than the CuFe-based catalysts under harsh conditions (Fig. 1C and S6). This demonstrates the PdFe catalyst shows high resistance to the sintering effect.

We also tried to investigate the influence of Fe₂O₃ particle size on the HAS activity. Downsizing the Fe₂O₃ particles would facilitate the construction of Pd-Fe₂O₃ interfaces. The Fe₂O₃ precursors with distinct particle sizes were prepared by the sol-gel method (Fig. S7-S8). Importantly, the PdFe-6.9 (37 nm) catalyst shows the best HAS performance, with HA selectivity of 26.5% and STY of 86.5 mg g_{cat}⁻¹ h⁻¹ under the reaction condition of 300 °C, 5 MPa, and 6 L g_{cat}⁻¹ h⁻¹ (Table S1). Such high performance has ranked the top among the ever-reported advanced Pd/Fe-based catalysts (Fig. 1D and Table S2). This encourages us to explore the nature of Pd-Fe interfaces under the real reaction conditions.

3.2. Identification of the PdFe-Fe₃C₂ interfaces

X-ray Diffraction (XRD) patterns of calcined PdFe-x catalysts prove PdO_x species is highly dispersed on Fe₂O₃ as discerned by no obvious diffractions of PdO_x (Fig. S9A). After H₂ reduction at 350 °C, the Fe₃O₄ crystal phase becomes dominant in the reduced catalysts, accompanied by the emergence of PdFe alloy at high Pd loading (Fig. S9B). The formation of PdFe alloy is further verified by the ~0.9° shift of Pd (111) and

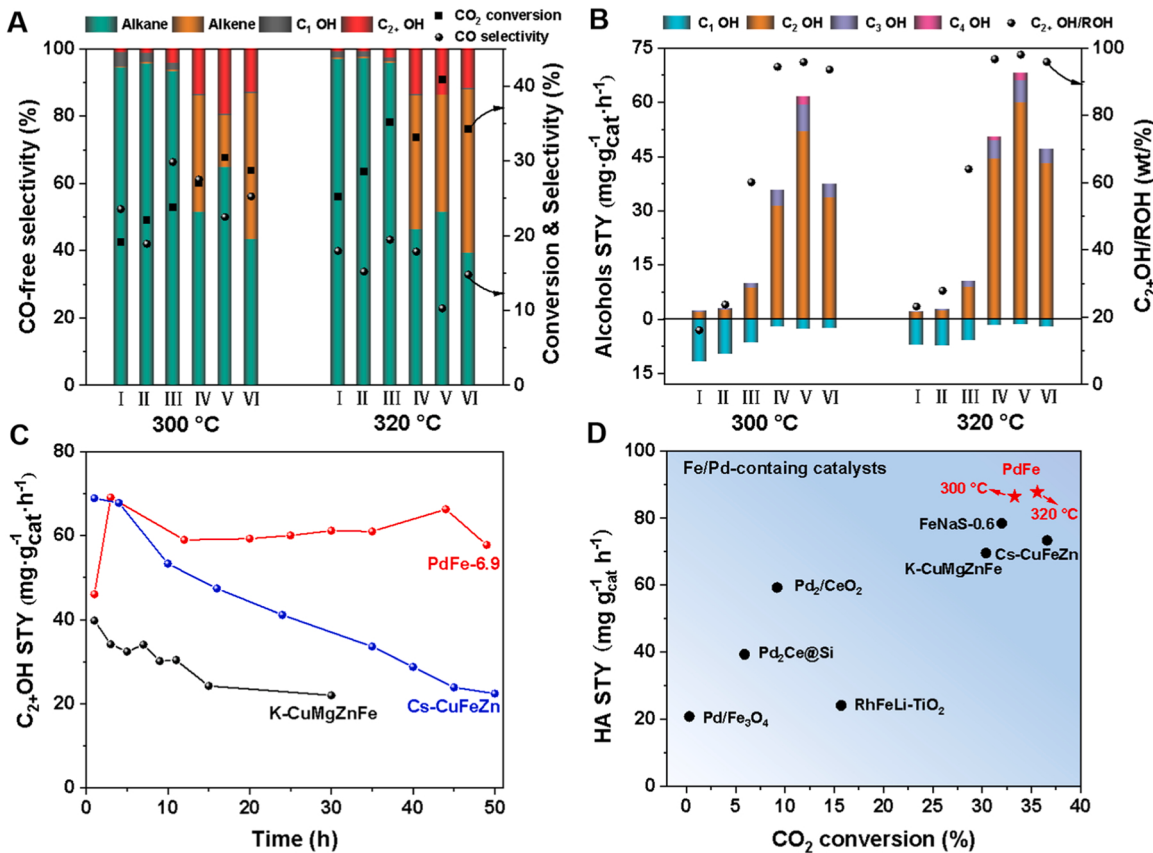


Fig. 1. Catalytic performance of various catalysts. (A) CO₂ conversion and product selectivity (C-mol%) and (B) distribution of alcohols in STY and mass fraction of C₂₊OH in total alcohols over PdFe-x catalysts with different Pd loading (I: 0, II: 0.1%, III: 0.9%, IV: 4.3%, V: 6.9%, VI: 10.4%). Reaction conditions: 300–320 °C, 5 MPa, H₂/CO₂/N₂ = 72/24/4, and GHSV of 6000 mL g_{cat}⁻¹ h⁻¹. (C) Accelerated deactivation test of PdFe-6.9 compared with the classical CuFe-based catalysts. Reaction conditions: 5 MPa, H₂/CO₂/N₂ = 72/24/4, 6000 mL g_{cat}⁻¹ h⁻¹ and 320 °C for PdFe-6.9; 6000 mL g_{cat}⁻¹ h⁻¹ and 300 °C for K-CuMgZnFe [21]; 4500 mL g_{cat}⁻¹ h⁻¹ and 330 °C for Cs-CuFeZn²². (D) Literature overview of the HAS performance (HA STY and CO₂ conversion) over Fe/Pd-containing catalysts.

(200) diffraction peaks in the spent PdFe-6.9 catalyst when compared to metallic Pd on γ -Al₂O₃ (Fig. 2A). Since the atomic radius of Fe is smaller than Pd, there happens to be a lattice contraction when generating PdFe alloy [31]. Transmission electron microscopy (TEM) images of the reduced PdFe-6.9 catalyst (Fig. S10) describe that Fe₃O₄ and PdFe alloy co-exist, and the PdFe alloy particles are relatively uniform with an average size of ~4.0 nm. The lattice *d*-spacing of 2.2 Å corresponds to the (111) planes of face-centered-cubic (fcc) PdFe nanoalloy, which is slightly lower than that of pure Pd crystal [32]. After catalytic reaction, the PdFe particles are uniformly distributed on the surface of iron support, and its average size marginally increases to ~5.4 nm (Fig. S11, see more discussion on the stability of the PdFe catalyst in SI). The formation of PdFe alloy is further confirmed by X-ray photoelectron spectroscopy (XPS) spectra (Fig. S12). The main Pd 3d band in the PdFe-x catalysts is located at high binding energy (335.3/340.6 eV) as compared to metallic Pd (335.0/340.3 eV) in the 6.9 Pd/ γ -Al₂O₃ catalyst. The increase of Pd 3d binding energy is attributed to the decrease of the energy level of the filled states on Pd after alloying. [31,33].

High-angle annular dark-field scanning transmission electron microscopy (HAADF-STEM) was utilized to further explore the fine structure of PdFe nanoalloy. As shown in STEM image and elemental mapping images of an individual PdFe alloy nanocrystal (Fig. 2B), the homogeneous distribution of Pd and Fe throughout the entire particle indicates Fe atoms permeate the lattice of Pd. Note that the relative concentration of Fe is higher at the surface than the bulk, due to the diffusion effect driven by chemical potential. The atomic ratio of Pd to Fe in the PdFe alloy nanocrystal was calculated to be 64:36 (Fig. S13A). Furthermore, the atomic resolution STEM image shows equal contrast/

brightness of atoms in the PdFe crystal (Fig. 2C), quite distinct from the alternating bright and dark contrasts in the ordered intermetallic compounds [32], indicating a disordered atomic arrangement in the PdFe alloy particle in our PdFe catalysts. The random arrangement of Pd/Fe atoms is further substantiated by the intensity profile along the line X-Y in the inverse FFT pattern of the magnified HAADF-STEM image (Fig. S13B).

In addition, we can find the presence of Fe₅C₂ phase, as well as the PdFe-Fe₅C₂ interfaces from STEM images of the spent PdFe-6.9 catalyst (Fig. 2D). The iron carbide phase is in situ formed from the carbonization of Fe species under reaction conditions. It is generally believed as the active site for CO dissociation and carbon chain propagation, which is also crucial to HAS [13,18,21,22,34–36]. From the XRD analyses of different noble metal catalysts (Ru, Ag) (Fig. S14) and PdFe-x catalysts (Fig. S15), only Pd with a certain loading (\geq 4.3 wt%) can easily promote the formation of Fe₅C₂ during the reaction process. The amount of Fe₅C₂ detected is in accord with the variation trend of chain-propagation probability (Fig. S2 and S3). XRD pattern of PdFe-6.9 after TOS test indicates PdFe alloy and Fe₅C₂ are in good stability (Fig. S16).

Considering that iron carbide is sensitive to air, we then conducted in situ XRD to study the real-time structural evolution of PdFe-6.9 catalyst. Pure Fe₂O₃ is used as a reference and it is totally transformed into Fe₃O₄ within 20 min during H₂ reduction (Fig. 3A). The diffraction at 44.6° belonging to α -Fe appears after 2 h reduction. When the gas is switched to CO₂/H₂ reaction gas, α -Fe is rapidly transformed into Fe₅C₂ in a short time accompanied by no obvious change in Fe₃O₄ crystal phase (Fig. 3B). By contrast, Fe₂O₃ in PdFe-6.9 is quickly converted into Fe₃O₄ within 10 min upon H₂ reduction (Fig. 3C). The accelerated

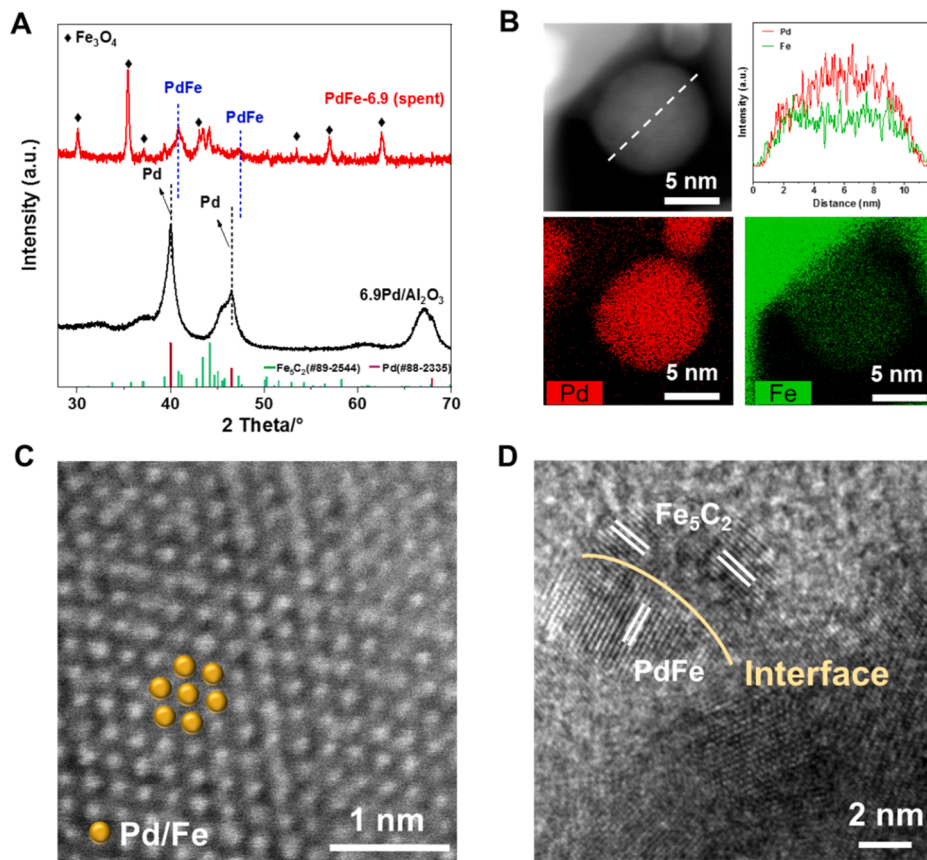


Fig. 2. Structural analysis of the PdFe-6.9 catalyst after reaction. (A) XRD analysis (6.9 Pd/Al₂O₃ as a reference). (B) HAADF-STEM, line scanning profile and elemental mapping (Pd and Fe) images of a PdFe alloy nanocrystal. (C) Atom-resolution HAADF-STEM image of PdFe (111) facet showing equal contrast/brightness of atoms. (D) TEM image showing the interface of PdFe alloy-Fe₅C₂.

transformation after Pd loading can be explained by the hydrogen spillover effect as indicated by H₂-TPR (Fig. S17) [37,38]. The slight lattice contraction of fcc-Pd from the shift of (111) diffraction reveals the generation of PdFe alloy phase. Considering that no metallic Fe is formed during the 3 h reduction, we believe that the reduced Fe atoms from Fe₃O₄ migrate onto Pd surface to form PdFe alloy rather than forming a separated phase of metallic Fe. Under CO₂ hydrogenation conditions, Fe₃O₄ can be rapidly and completely converted into Fe₅C₂ within 30 min (Fig. 3D and Fig. S18), and the carbonization time is further shortened to 20 min when the Pd content was increased to 10.4% (Fig. S19). As a control experiment, the physically mixed catalyst of 6.9 Pd/γ-Al₂O₃ + Fe₂O₃ (no activity in HAS) possesses neither Fe₅C₂ species nor PdFe alloy after CO₂ hydrogenation reaction (Fig. S20 and S21), which highlights the pivotal role of PdFe alloy in iron carbidization. Therefore, we conclude that PdFe alloy induces the formation of Fe₅C₂, thus creating abundant PdFe alloy-Fe₅C₂ interfaces.

3.3. Chemisorption analyses of H₂ and CO₂

H₂-TPD-MS results show the desorption capacity of H₂ over PdFe-6.9 decreases obviously when compared with 6.9 Pd/γ-Al₂O₃ (Fig. S22). This indicates that the hydrogenation ability decreases sharply after Pd alloying. Generally, the strong hydrogenation ability of noble metals (e.g., Pt, Pd, and Ru) originates from the moderate H* adsorption free energy. When Pd is alloyed with Fe (lattice contraction), the energy level of filled Pd 4d valence orbitals would decrease, accompanied by the upshift of unoccupied Pd 4d orbitals [39,40]. According to the d-band center theory, the down-shift of Pd 4d band center results in the weakening of Pd-adsorbate binding [41,42]. Thus, the chemisorption of H* on PdFe alloy is disfavored, as also supported by the decrease of the

onset H₂ desorption temperature after alloying. It is believed that the diminished hydrogenation capability is beneficial to stabilizing the iron carbide active phase via maintaining high coverage of dissociated C* species on the catalyst surface. The excessive hydrogen capability would cause the fast consumption of surface C* species and thus produce massive methane in the products, as we did not detect any Fe₅C₂ phase in the physically mixed catalyst of 6.9 Pd/γ-Al₂O₃ + Fe₂O₃ after reaction (Fig. S21).

We also find that, after Pd loading on Fe₂O₃, the CO₂ desorption capacity is significantly enhanced as shown in CO₂-TPD-MS profiles (Fig. S23). This indicates that the Pd modification increases the density of basic sites on catalyst surface, accommodating an increasing number of CO₂ molecules. Raising the CO₂ coverage would favor the conversion of CO₂ (Fig. 1). The desorption peak area ratio of H₂ to CO₂ as a descriptor can reflect the adsorbed H/C ratio on the catalyst surface. When increasing Pd loading, the surface H/C ratio drops significantly, which is beneficial to C-C coupling reaction, facilitating the production of HA and olefins (Table 1). Moreover, the low H/C ratio is also important for the carbidization of Fe caused by the improved carbon chemical potential which can be demonstrated by the fast carbonization rate of PdFe-10.4 from the in situ XRD results (Fig. S19). This is the first example of deep iron carbidization induced by transition metal/alloy rather than the assistance of alkali ion promoters. It is interesting to note that the in situ generated PdFe alloy seems to unconventionally resemble alkali metal promoters in the role of regulating the adsorption/activation of H₂ and CO₂ over Fe or Co based FTS catalysts [43–45]. Alkali promoters have been shown to accelerate iron carbidization under CO₂ hydrogenation conditions, probably due to the weakened hydrogenation capability and enhanced reaction rate of RWGS [7]. On the basis of the above analyses, we are confident that the iron

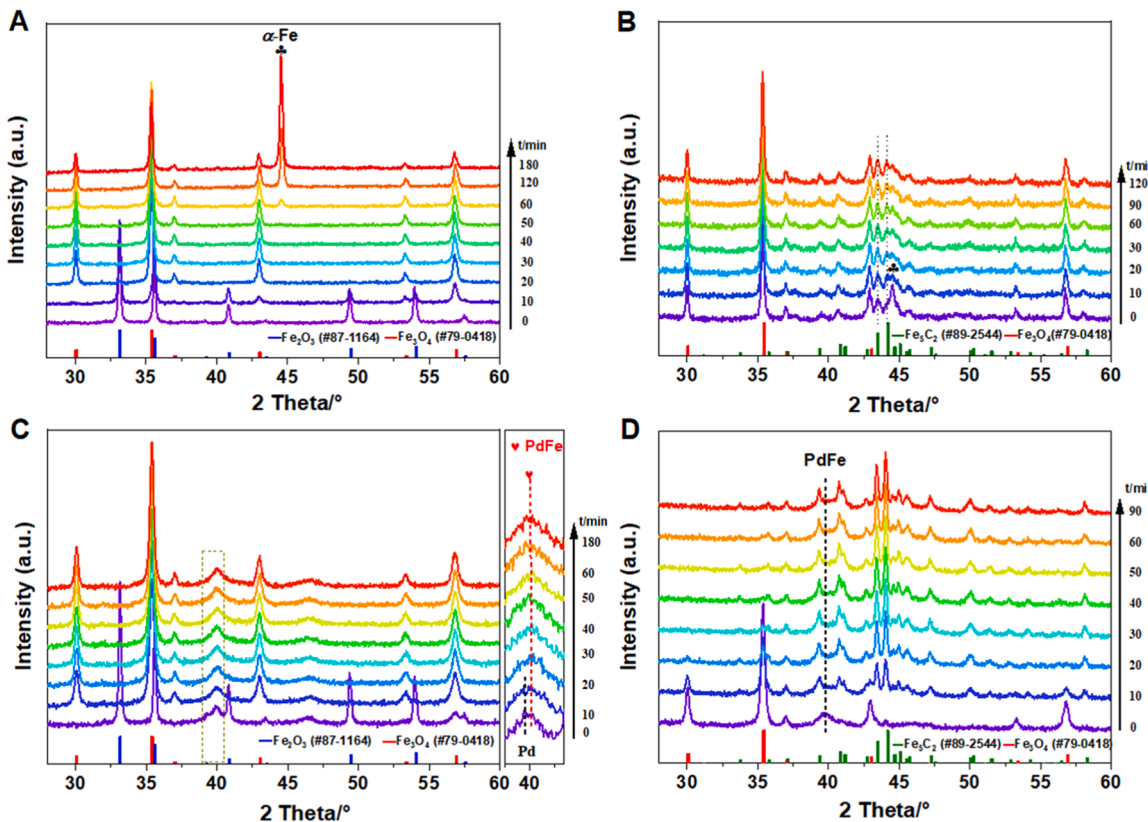


Fig. 3. In situ XRD characterizations under different atmosphere. (A, B) Fe_2O_3 and (C, D) PdFe-6.9. Reaction conditions: (A, C) 350 °C, 10% H_2/N_2 , 1 bar; (B, D) 320 °C, $\text{CO}_2/\text{H}_2 = 1/3$, 8 bar.

Table 1
The related desorption area of CO_2/H_2 -TPD-MS and product selectivity.

Catalysts	A_{CO_2} (*E-8 a.u.) ^a	A_{H_2} (*E-7 a.u.) ^b	$A_{\text{H}_2}/A_{\text{CO}_2}^c$	RH ^d =HA Select. (%)
Fe_2O_3	1.4	3.5	25.0	1.3
PdFe-0.1	5.1	3.2	6.3	1.4
PdFe-6.9	8.4	2.3	2.7	48.3
PdFe-	17	2.7	1.6	60.4
10.4				

[a] Desorption peak area of CO_2 in CO_2 -TPD-MS.

[b] Desorption peak area of H_2 in H_2 -TPD-MS.

[c] The ratio of A_{H_2} and A_{CO_2} .

[d] Selectivity of olefins and HA at 320 °C.

carbidization induced by adjacent PdFe alloy is tightly linked with the regulation effect on the adsorptive activation of H_2 and CO_2 , which further tailor the reaction network of CO_2 hydrogenation.

3.4. Mechanistic study on HAS at the PdFe- Fe_5C_2 interfaces

We next conducted in situ diffuse reflectance infrared Fourier transform spectroscopy (DRIFTS) of the $\text{CO}_2 + \text{H}_2$ reaction over the PdFe-6.9 catalyst. Gaseous CO (2112 and 2180 cm^{-1}) appears immediately after exposure to CO_2/H_2 (Fig. 4A) [46,47]. Subsequently, the bands for $\text{C}_2\text{H}_5\text{O}^*$ species (1038 , 2856 , 2926 , 2956 cm^{-1}) start to emerge and gradually intensify with reaction time (Fig. 4B and S24) [48–50]. We can also find a small amount of gaseous CH_4 (3015 cm^{-1}) from CO dissociation/hydrogenation. The dynamic change of these intermediates (Fig. 4C) proves the CO-mediated reaction pathway for HAS. In situ DRIFTS spectra of CO_2 hydrogenation over pure Fe_2O_3 and PdFe-0.1 as references were also conducted for comparison. Over the two catalysts, gaseous CH_4 is dominant when compared to alkyl species

(νCH_2 and νCH_3) and gaseous CO (Fig. 4D, S25 and S26). There is almost no presence of $\nu(\text{C}-\text{O})$ band, implying that pure Fe catalyst or even doped with trace Pd does not catalyze alcohol synthesis. In contrast, PdFe-6.9 is capable of inhibiting the methanation reaction by suppressing the hydrogenation capability (H-D exchange experiments in Fig. S27), thus facilitating the C-C coupling of CH_x and CO species to give oxygenated products. Moreover, the fast accumulation of CO species from RWGS reaction (Fig. 4C) is also beneficial to CO insertion. Considering that abundant PdFe- Fe_5C_2 interfacial sites exist in the PdFe-6.9 catalyst under reaction conditions, we are confident that the HAS is strongly relevant to the PdFe- Fe_5C_2 interfaces.

We next prepared the single phase of PdFe alloy (disordered solid solution) supported on SBA-15 (Fig. S28) and investigated its catalytic behaviors in CO_2 hydrogenation (Fig. S29). It is found that the PdFe alloy catalyst is mainly favorable for RWGS reaction (>75% selectivity) at 300–320 °C. And the CO_2 conversion is more than twice that of Pd/ Al_2O_3 catalyst, indicating that PdFe alloy is more active than metallic Pd in RWGS reaction. According to the Blyholder model of CO adsorption, lowering the d band center of Pd 4d would reduce the back donation of electrons from the valence d states to the π^* orbital of CO, resulting in the weakening of Pd-CO binding [51]. The DRIFTS spectra of CO adsorption (Fig. S30) describe that alloying Pd with Fe would cause the disappearance of adsorbed CO band remarkably, further revealing the Pd-CO binding is weakened after alloying. It is well known that Pt-group metals are easily poisoned by CO due to the strong CO adsorption [52]. Diminishing the CO binding by Pd alloying favors CO desorption, thus facilitating RWGS reaction (Fig. S29). On the other hand, the weakened CO binding over PdFe alloy would be also beneficial to the CO insertion reaction. The in situ DRIFTS analysis of ethylene carbonylation reaction over PdFe/SBA-15 demonstrated that PdFe alloy is responsible for CO insertion to give C_{2+} alcohols (Fig. S31). We also performed CO-TPSR experiment, the ability of CO non-dissociative activation becomes

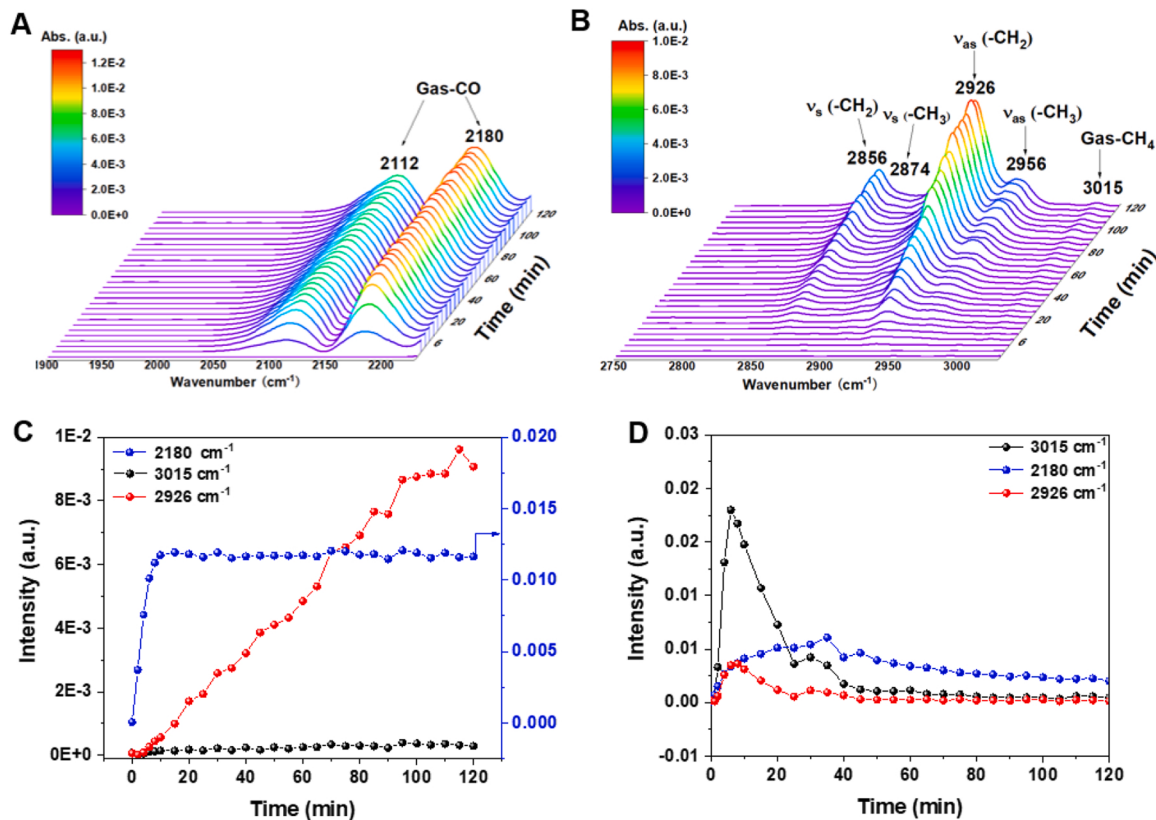


Fig. 4. In situ DRIFTS spectra of the CO_2 hydrogenation reaction. Spectra in the range of (A) 1900–2230 cm^{-1} and (B) 2750–3030 cm^{-1} for the PdFe-6.9 catalyst. Reaction conditions: 280 °C, 3 bar, $\text{CO}_2/\text{H}_2 = 1/3$, and 30 mL min^{-1} . Dynamic change of the IR band intensity of ν_{as} (C-H) (2926 cm^{-1}), $\nu(\text{CH}_4)$ (3015 cm^{-1}) and ν (CO) (2180 cm^{-1}) over (C) PdFe-6.9 compared with (D) Fe_2O_3 .

stronger along with the increase of PdFe alloy content from 0.1% to 10.4% (Fig. S32 and Table S3). The CO pulse transient hydrogenation experiment at H_2/Ar atmosphere illustrated that PdFe- Fe_5C_2 interfaces are crucial for C-C coupling (Fig. S33–S35). Therefore, we believe that the PdFe alloy can play a role of CO production and subsequent non-dissociative activation and the PdFe- Fe_5C_2 interfaces render the C-C coupling of alkyl and CO species in catalyzing CO_2 -to-HA reaction (see more discussion on the synergy of PdFe- Fe_5C_2 interfaces in SI).

4. Conclusion

In summary, we have demonstrated the in situ fabrication of PdFe alloy- Fe_5C_2 interfaces as active sites for efficient and stable HAS from CO_2 hydrogenation. The PdFe alloy plays a pivotal role in regulating the adsorptive activation of H_2 and CO_2 , and thus induces the complete transformation of Fe species to Fe_5C_2 , forming abundant PdFe alloy- Fe_5C_2 interfacial sites. The in situ DRIFTS analysis reveals the CO-mediated reaction pathway for HAS. PdFe alloy is responsible for RWGS reaction and CO non-dissociative activation, while Fe_5C_2 is in charge of CO dissociation and carbon chain propagation. The well-defined PdFe alloy- Fe_5C_2 interfaces endue HAS via C-C coupling of adsorbed alkyl and CO species, with the HA STY of 86.5 mg g $_{\text{cat}}^{-1}$ h $^{-1}$ and HA selectivity of 26.5% over the optimized PdFe catalyst. The accelerated deactivation test unveils that the PdFe-6.9 catalyst exhibits better durability than the widely studied CuFe-based catalysts under harsh conditions. This work will stimulate more attempts to discover new-type catalysts with well-defined structures for efficient and stable CO_2 hydrogenation to HA.

CRediT authorship contribution statement

Tangkang Liu: Formal analysis, Methodology. Mingrui Wang:

Methodology. Xinxin Zhang: Conceptualization, Data curation, Formal analysis, Validation, Visualization. Ying Zhou: Conceptualization, Data curation, Formal analysis, Investigation, Methodology, Validation, Visualization, Writing – original draft. Yanqiu Wang: Conceptualization, Data curation, Formal analysis, Investigation, Methodology, Validation, Visualization, Writing – original draft. Guoliang Liu: Conceptualization, Funding acquisition, Methodology, Project administration, Resources, Supervision, Writing – review & editing. Xinlin Hong: Conceptualization, Project administration, Resources, Supervision. Guanghui Zhang: Methodology, Writing – review & editing. Jinxing Wei: Formal analysis, Methodology.

Declaration of Competing Interest

The authors declare that they have no known competing financial interests or personal relationships that could have appeared to influence the work reported in this paper.

Data availability

Data will be made available on request.

Acknowledgments

This work is financially supported by the National Natural Science Foundation of China (22172113), the Fundamental Research Funds for the Central Universities (2042022kf1178), and the Natural Science Foundation of Hubei Province of China (2021CFB358).

Appendix A. Supporting information

Supplementary data associated with this article can be found in the

online version at doi:10.1016/j.apcatb.2024.123691.

References

- [1] A. Alvarez, A. Bansode, A. Urakawa, A.V. Bavykina, T.A. Wezendonk, M. Makkee, J. Gascon, F. Kapteijn, Challenges in the greener production of formates/formic acid, methanol, and DME by heterogeneously catalyzed CO₂ hydrogenation processes, *Chem. Rev.* 117 (2017) 9804–9838.
- [2] J.J. Spivey, A. Egbebi, Heterogeneous catalytic synthesis of ethanol from biomass-derived syngas, *Chem. Soc. Rev.* 36 (2007) 1514–1528.
- [3] J. Goldemberg, Ethanol for a sustainable energy future, *Science* 315 (2007) 808–810.
- [4] M. Ao, G. Pham, J. Sunarso, M. Tade, S. Liu, Active centers of catalysts for higher alcohol synthesis from syngas: a review, *ACS Catal.* 8 (2018) 7025–7050.
- [5] Y. Yang, L. Wang, K. Xiao, T. Zhao, H. Wang, L. Zhong, Y. Sun, Elucidation of reaction network of higher alcohol synthesis over modified FT catalysts by probe molecule experiments, *Catal. Sci. Technol.* 5 (2015) 4224–4232.
- [6] T. Lin, X. Qi, X. Wang, L. Xia, C. Wang, F. Yu, H. Wang, S. Li, L. Zhong, Y. Sun, Direct production of higher oxygenates by syngas conversion over a multifunctional catalyst, *Angew. Chem. Int. Ed.* 58 (2019) 4627–4631.
- [7] D. Xu, Y. Wang, M. Ding, X. Hong, G. Liu, S.C.E. Tsang, Advances in higher alcohol synthesis from CO₂ hydrogenation, *Chem* 7 (2021) 849–881.
- [8] Y. Wang, D. Xu, X. Zhang, X. Hong, G. Liu, Selective C₂₊ alcohol synthesis by CO₂ hydrogenation via a reaction-coupling strategy, *Catal. Sci. Technol.* 12 (2022) 1539–1550.
- [9] Y. Wang, K. Wang, B. Zhang, X. Peng, X. Gao, G. Yang, H. Hu, M. Wu, N. Tsubaki, Direct conversion of CO₂ to ethanol boosted by intimacy-sensitive multifunctional catalysts, *ACS Catal.* 11 (2021) 11742–11753.
- [10] T. Inoue, T. Iizuka, K. Tanabe, Hydrogenation of carbon-dioxide and carbon-monoxide over supported rhodium catalysts under 10 Bar pressure, *Appl. Catal.* 46 (1989) 1–9.
- [11] L. Wang, L. Wang, J. Zhang, X. Liu, H. Wang, W. Zhang, Q. Yang, J. Ma, X. Dong, S. J. Yoo, J.-G. Kim, X. Meng, F.-S. Xiao, Selective hydrogenation of CO₂ to ethanol over cobalt catalysts, *Angew. Chem. Int. Ed.* 57 (2018) 6104–6108.
- [12] S. Zhang, Z. Wu, X. Liu, Z. Shao, L. Xia, L. Zhong, H. Wang, Y. Sun, Tuning the interaction between Na and Co₂C to promote selective CO₂ hydrogenation to ethanol, *Appl. Catal. B* 293 (2021) 120207.
- [13] Y. Li, W. Gao, M. Peng, J. Zhang, J. Sun, Y. Xu, S. Hong, X. Liu, X. Liu, M. Wei, B. Zhang, D. Ma, Interfacial Fe₅C₂-Cu Catalysts toward low-pressure syngas conversion to long-chain alcohols, *Nat. Commun.* 11 (2020) 61.
- [14] K.K. Bando, N. Ichikuni, K. Soga, K. Kunimori, H. Arakawa, K. Asakura, Characterization of Rh particles and Li-promoted Rh particles in Y zeolite during CO₂ hydrogenation—a new mechanism for catalysis controlled by the dynamic structure of Rh particles and the Li additive effect, *J. Catal.* 194 (2000) 91–104.
- [15] H. Kusama, K. Okabe, K. Sayama, H. Arakawa, CO₂ hydrogenation to ethanol over promoted Rh/SiO₂ catalysts, *Catal. Today* 28 (1996) 261–266.
- [16] C. Yang, S. Liu, Y. Wang, J. Song, G. Wang, S. Wang, Z. Zhao, R. Mu, J. Gong, The interplay between structure and product selectivity of CO₂ hydrogenation, *Angew. Chem. Int. Ed.* 58 (2019) 11242–11247.
- [17] H. Luk, C. Mondelli, S. Mitchell, S. Siol, J. Stewart, D. Ferre, J. Perez-Ramirez, Role of carbonaceous supports and potassium promoter on higher alcohols synthesis over copper-iron catalysts, *ACS Catal.* 8 (2018) 9604–9618.
- [18] R. Yao, J. Wei, Q. Ge, J. Xu, Y. Han, Q. Ma, H. Xu, J. Sun, Monometallic iron catalysts with synergistic Na and S for higher alcohols synthesis via CO₂ hydrogenation, *Appl. Catal. B* 298 (2021) 120556.
- [19] J. Zhu, P. Wang, X. Zhang, G. Zhang, R. Li, W. Li, T.P. Senftle, W. Liu, J. Wang, Y. Wang, A. Zhang, Q. Fu, C. Song, X. Guo, Dynamic structural evolution of iron catalysts involving competitive oxidation and carburization during CO₂ hydrogenation, *Sci. Adv.* 8 (2022) eabm3629.
- [20] G. Prieto, Carbon dioxide hydrogenation into higher hydrocarbons and oxygenates: thermodynamic and kinetic bounds and progress with heterogeneous and homogeneous catalysis, *ChemSusChem* 10 (2017) 1056–1070.
- [21] D. Xu, M. Ding, X. Hong, G. Liu, Mechanistic aspects of the role of k promotion on Cu-Fe-based catalysts for higher alcohol synthesis from CO₂ hydrogenation, *ACS Catal.* 10 (2020) 14516–14526.
- [22] D. Xu, M. Ding, X. Hong, G. Liu, S.C.E. Tsang, Selective C₂₊ alcohol synthesis from direct CO₂ hydrogenation over a Cs-promoted Cu-Fe-Zn catalyst, *ACS Catal.* 10 (2020) 5250–5260.
- [23] X. Jiang, X. Nie, X. Guo, C. Song, J.G. Chen, Recent advances in carbon dioxide hydrogenation to methanol via heterogeneous catalysis, *Chem. Rev.* 120 (2020) 7984–8034.
- [24] Y. Lou, F. Jiang, W. Zhu, L. Wang, T. Yao, S. Wang, B. Yang, B. Yang, Y. Zhu, X. Liu, CeO₂ supported Pd dimers boosting CO₂ hydrogenation to ethanol, *Appl. Catal. B* 291 (2021) 120122.
- [25] F.J. Caparrós, L. Soler, M.D. Rossell, I. Angurell, L. Piccolo, O. Rossell, J. Llorca, Remarkable carbon dioxide hydrogenation to ethanol on a palladium/iron oxide single-atom catalyst, *ChemCatChem* 10 (2018) 2365–2369.
- [26] J. Chen, Y. Zha, B. Liu, Y. Li, Y. Xu, X. Liu, Rationally designed water enriched nano reactor for stable CO₂ hydrogenation with Near 100% ethanol selectivity over diatomic palladium active sites, *ACS Catal.* 13 (2023) 7110–7121.
- [27] H. Zhang, S. Wang, K. Jiang, T. Andre, W.B. Cai, In situ spectroscopic investigation of CO accumulation and poisoning on Pd black surfaces in concentrated HCOOH, *J. Power Sources* 199 (2012) 165–169.
- [28] A.P. Tsai, S. Kameoka, K. Nozawa, M. Shimoda, Y. Ishii, Intermetallic: a pseudoelement for catalysis published as part of the accounts of chemical research special issue "advancing chemistry through intermetallic compounds", *Acc. Chem. Res.* 50 (2017) 2879–2885.
- [29] A.P. Tsai, S. Kameoka, Y. Ishii, PdZn=Cu: can an intermetallic compound replace an element? *J. Phys. Soc. Jpn.* 73 (2004) 3270–3273.
- [30] M. Gong, T. Shen, Z. Deng, H. Yang, Z. Li, J. Zhang, R. Zhang, Y. Hu, X. Zhao, H. Xin, D. Wang, Surface engineering of PdFe ordered intermetallics for efficient oxygen reduction electrocatalysis, *Chem. Eng. J.* 408 (2021) 127297.
- [31] M.A. Matin, J.H. Jang, Y.U. Kwon, PdM nanoparticles (M = Ni, Co, Fe, Mn) with high activity and stability in formic acid oxidation synthesized by sonochemical reactions, *J. Power Sources* 262 (2014) 356–363.
- [32] L. Luo, M. Wang, Y. Cui, Z. Chen, J. Wu, Y. Cao, J. Luo, Y. Dai, W.-X. Li, J. Bao, J. Zeng, Surface iron species in palladium–iron intermetallic nanocrystals that promote and stabilize CO₂ methanation, *Angew. Chem. Int. Ed.* 59 (2020) 14434–14442.
- [33] E. Castillejos-Lopez, G. Agostini, M. Di Michel, A. Iglesias-Juez, B. Bachiller-Baeza, Synergy of contact between ZnO surface planes and PdZn nanostructures: morphology and chemical property effects in the intermetallic sites for selective 1,3-butadiene hydrogenation, *ACS Catal.* 7 (2017) 796–811.
- [34] P. Zhai, C. Xu, R. Gao, X. Liu, M. Li, W. Li, X. Fu, C. Jia, J. Xie, M. Zhao, X. Wang, Y. Li, Q. Zhang, X. Wen, D. Ma, Highly tunable selectivity for syngas-derived alkenes over zinc and sodium-modulated Fe₅C₂ catalyst, *Angew. Chem. Int. Ed.* 55 (2016) 9902–9907.
- [35] F. Lu, X. Chen, W. Wang, Y. Zhang, Adjusting the CO₂ hydrogenation pathway via the synergic effects of iron carbides and iron oxides, *Catal. Sci. Technol.* 11 (2021) 7694–7703.
- [36] S. Li, H. Guo, C. Luo, H. Zhang, L. Xiong, X. Chen, L. Ma, Effect of iron promoter on structure and performance of K/Cu–Zn catalyst for higher alcohols synthesis from CO₂ hydrogenation, *Catal. Lett.* 143 (2013) 345–355.
- [37] B. Hu, Y. Yin, G. Liu, S. Chen, X. Hong, S.C.E. Tsang, Hydrogen spillover enabled active Cu sites for methanol synthesis from CO₂ hydrogenation over Pd doped CuZn catalysts, *J. Catal.* 359 (2018) 17–26.
- [38] K. Waiz, S. Clelia, K. Armin, G. Jens, V. Joost, E. Yasin, B. Jeroen, A Catalyst support effects on hydrogen spillover, *Nature* 541 (2017) 68–71.
- [39] V.J. Cybulskis, B.C. Bukowski, H.-T. Tseng, J.R. Gallagher, Z. Wu, E. Wegener, A. J. Kropf, B. Ravel, F.H. Ribeiro, J. Greeley, J.T. Miller, Zinc promotion of platinum for catalytic light alkane dehydrogenation: insights into geometric and electronic effects, *ACS Catal.* 7 (2017) 4173–4181.
- [40] C. Yang, Z. Wu, G. Zhang, H. Sheng, J. Tian, Z. Duan, H. Sohn, A. Kropf, T.P. Wu, T. Krause, J. Miller, Promotion of Pd nanoparticles by Fe and formation of a Pd₃Fe intermetallic alloy for propane dehydrogenation, *Catal. Today* 323 (2019) 123–128.
- [41] B. Hammer, J.K. Norskov, Theoretical surface science and catalysis-calculations and concepts, *Adv. Catal.* 45 (2000) 71–129.
- [42] L.A. Kibler, A.M. El-Aziz, R. Hoyer, D.M. Kolb, Tuning reaction rates by lateral strain in a palladium monolayer, *Angew. Chem. Int. Ed.* 44 (2005) 2080–2084.
- [43] H. Xiong, M.A. Motchelaho, M. Moyo, L.L. Jewell, N.J. Coville, I alkali metal promoters on Fe/CNT catalysts in Fischer-Tropsch synthesis, *Fuel* 150 (2015) 687–696.
- [44] Z. Li, N. Yao, J. Cen, X. Li, L. Zhong, Y. Sun, M. He, Effects of alkali metal promoters on the structure-performance relationship of CoMn catalysts for Fischer-Tropsch synthesis, *Catal. Sci. Technol.* 10 (2020) 1816–1826.
- [45] P. Zhai, Y. Li, M. Wang, J. Liu, Z. Cao, J. Zhang, Y. Xu, X. Liu, Y. Li, Q. Zhu, D. Xiao, X. Wen, D. Ma, Development of direct conversion of syngas to unsaturated hydrocarbons based on Fischer-Tropsch route, *Chem* 7 (2021) 3027–3051.
- [46] K.I. Hadjiliavan, G.N. Vayssilov, Characterization of oxide surfaces and zeolites by carbon monoxide as an IR probe molecule, *Adv. Catal.* 47 (2002) 307–511.
- [47] F. Solymosi, E. Novak, A. Molnar, Infrared spectroscopic study on co-induced structural-changes of iridium on an alumina support, *J. Phys. Chem.* 94 (1990) 7250–7255.
- [48] D. Xu, H. Yang, X. Hong, G. Liu, S.C.E. Tsang, Tandem catalysis of direct CO₂ hydrogenation to higher alcohols, *ACS Catal.* 11 (2021) 8978–8984.
- [49] J.V. Ochoa, C. Trevisanut, J.M.M. Millet, G. Busca, F. Cavani, In situ DRIFTS-MS study of the anaerobic oxidation of ethanol over spinel mixed oxides, *J. Phys. Chem. C* 117 (2013) 23908–23918.
- [50] L. Ding, T. Shi, J. Gu, Y. Cui, Z. Zhang, C. Yang, T. Chen, M. Lin, P. Wang, N. Xue, L. Peng, X. Guo, Y. Zhu, Z. Chen, W. Ding, CO₂ hydrogenation to ethanol over Cu@Na-beta, *Chem* 6 (2020) 2673–2689.
- [51] B. Hammer, Y. Morikawa, J.K. Norskov, Chemisorption at metal surfaces and overlayers, *Phys. Rev. Lett.* 76 (1996) 2141–2144.
- [52] J. Shim, J. Lee, Y. Ye, J. Hwang, S.K. Kim, T.H. Lim, U. Wiesner, J. Lee, One-pot synthesis of intermetallic electrocatalysts in ordered, large-pore mesoporous carbon/silica toward formic acid oxidation, *ACS Nano* 6 (2012) 6870–6881.